
VIRTUAL SENSING FOR REAL-TIME DEGRADATION MONITORING OF NUCLEAR SYSTEMS: LEVERAGING DEEPONET FOR ENHANCED SENSING COVERAGE FOR DIGITAL TWIN-ENABLING TECHNOLOGY

PREPRINT

Raisa Bentay Hossain

Nuclear, Plasma & Radiological Engineering
 University of Illinois at Urbana-Champaign
 Urbana, IL 61801, USA
 rh33@illinois.edu

Farid Ahmed

Nuclear, Plasma & Radiological Engineering
 University of Illinois at Urbana-Champaign
 Urbana, IL 61801, USA

Kazuma Kobayashi

Nuclear, Plasma & Radiological Engineering
 University of Illinois at Urbana-Champaign
 Urbana, IL 61801, USA
 kazumak2@illinois.edu

Seid Koric

National Center for Supercomputing Applications
 University of Illinois at Urbana-Champaign
 Urbana, IL 61801, USA
 koric@illinois.edu

Diab Abueidda

National Center for Supercomputing Applications
 University of Illinois at Urbana-Champaign
 New York University Abu Dhabi
 United Arab Emirates
 abueidd2@illinois.edu

Syed Bahauddin Alam

Nuclear, Plasma & Radiological Engineering
 National Center for Supercomputing Applications
 University of Illinois at Urbana-Champaign
 Urbana, IL 61801, USA
 alams@illinois.edu

October 18, 2024

ABSTRACT

Effective real-time monitoring technique is crucial for detecting material degradation and maintaining the structural integrity of nuclear systems to ensure both safety and operational efficiency. Traditional physical sensor systems face limitations such as installation challenges, high costs, and difficulties in measuring critical parameters in hard-to-reach or harsh environments, often resulting in incomplete data coverage. Machine learning-driven virtual sensors offer a promising solution by enhancing physical sensor capabilities to monitor critical degradation indicators like pressure, velocity, and turbulence. However, conventional machine learning models struggle with real-time monitoring due to the high-dimensional nature of reactor data and the need for frequent retraining. This paper explores the use of Deep Operator Networks (DeepONet) within a digital twin (DT) framework to predict key thermal-hydraulic parameters in the hot leg of an AP-1000 Pressurized Water Reactor (PWR). In this study, DeepONet is trained with different operational conditions, which relaxes the requirement of continuous retraining, making it suitable for online and real-time prediction components for DT. Our results show that DeepONet achieves accurate predictions with low mean squared error and relative L2 error and can make predictions on unknown data *160,000 times faster than traditional finite element (FE) simulations*. This speed and accuracy make DeepONet a powerful tool for tracking conditions that contribute to material degradation in real-time, enhancing reactor safety and longevity.

1 Introduction

Proper monitoring and inspection of in-service components in nuclear reactors is essential for long-term safety and efficiency, as these components are continuously subjected to extreme temperatures, pressures, and radiation. Among these components, the primary circuit is particularly important, as it removes the immense heat generated in the reactor core, acting as the central component of reactor cooling system. This loop carries highly pressurized water at high velocities, creating significant mechanical stresses on the piping system Zou and Derreberry [2020], Keller and Bilanin [2002]. Turbulent coolant flow, especially in areas with bends and joints, leads to localized disturbances Tunstall and Harvey [1968], Dutta et al. [2016], Shimizu et al. [1992] that can induce material degradation mechanisms such as erosion, fatigue, and stress corrosion cracking. Given the critical role of the primary coolant loop, real-time monitoring is essential for detecting early signs of degradation and preventing failures. Tracking key parameters—pressure, velocity, and turbulence—allows operators to identify anomalies such as flow reductions, vibrations, and pressure drops. These insights provide early warnings, often before structural damage occurs, ensuring safe and efficient reactor operation while reducing risks associated with material degradation.

Traditionally, nuclear reactors employ non-destructive testing (NDT) methods, including eddy-current, ultrasonic, radiographic, and visual inspections, to detect degradation in the piping system Khan et al. [2023]. These methods are effective at identifying various forms of material degradation, including cracks, corrosion, and fatigue, without causing damage to the system itself. However, these processes are usually carried out through scheduled outages, leading to significant revenue losses. In addition, nuclear piping systems often extend over several miles, making it challenging to inspect the entire system within the limited outage period Sandhu et al. [2024]. As a result, while traditional NDT methods remain valuable, they present challenges in terms of achieving comprehensive system coverage and addressing material degradation during routine operations. Real-time monitoring of coolant flow offers an alternative to these scheduled inspections. If during real time monitoring, anomalies or significant deviations from normal parameters are observed, inspections can be scheduled promptly to address specific concerns. This approach not only enhances the safety and reliability of the reactor but also minimizes the need for extensive and costly scheduled outages, as regular scheduled inspections can be replaced by conditional inspections only when there is a clear indication of potential problems Han et al. [2022].

Current methods for real-time coolant flow monitoring in nuclear reactors include ultrasonic, electromagnetic, thermal dispersion, vortex, and differential pressure flow meters Davydov et al. [2021], Tokarz [1983]. Additionally, sensors for temperature, pressure, radiation, and chemical composition are placed throughout the coolant piping system to ensure continuous monitoring Kuroze et al. [1996], Lister and Uchida [2015], Jensen et al. [1996]. These sensors are typically located at the inlet and outlet of the reactor core, steam generators, and other components U.S. Nuclear Regulatory Commission [2011]. When placing sensors, factors such as radiation, temperature, and pressure must be carefully considered to ensure optimal performance and minimize sensor degradation Hossain et al. [2024], Karnik et al. [2024]. While the current sensor network for monitoring coolant flow in nuclear reactors provides extensive coverage, ensuring the reactors function properly, there are still a lot of opportunities for further improvement. The main issue with relying solely on physical sensors is the high installation, calibration, and maintenance costs, along with unmonitored areas that create potential blind spots for undetected anomalies. Ideally, sensors would be placed at regular intervals along the piping system for comprehensive monitoring, but this is impractical due to flow disturbances and logistical challenges. While placing sensors at the inlet and outlet of piping segments is feasible, installing them within pipe sections is difficult. Even when sensors are installed and calibrated, failures can complicate detection and replacement, adding operational challenges of relying on extensive physical sensor networks.

To address these limitations, Distributed Fiber Optic (DFO) sensing has emerged as a promising alternative, having been explored for decades in nuclear plants to monitor temperature, flow, and pressure Wu et al. [2021], Ferdinand et al. [2000]. Another innovative solution is the use of virtual sensors—software-based models that estimate physical quantities using data and simulations rather than direct physical measurements Zhao et al. [2024a,b], Niresi et al. [2024]. These virtual sensors mimic the behavior of physical sensors, providing readings without requiring the installation of actual hardware Sun et al. [2017], Masti et al. [2021], Ofner et al. [2023]. They are especially useful in situations where physical placement is not feasible because of limited space or unfavorable weather Ahmed et al. [2013]. When used in conjunction with other sensors that are keeping an eye on the same conditions, virtual sensors improve data reliability by reducing signal interference Liu et al.. Virtual sensors are easily adjustable to meet changing needs, unlike real sensors that require actual modifications Barmaz [2023]. The concept of virtual sensors in the nuclear sector is relatively new but not entirely unfamiliar. Sevilla et al. Sevilla and Pulido [1998] demonstrate how neural networks can estimate variables in pressurized water reactors by optimizing input selection and network architecture. Ahmed et al. Ahmed et al. [2013] develop virtual sensor networks for accident monitoring in nuclear power plants using statistical relationships among process parameters. Tipireddy et al. Tipireddy et al. [2017] present virtual sensors with Gaussian process models to temporarily replace faulty sensors in nuclear power plants, ensuring accurate measurements and reducing unscheduled shutdowns.

When it comes to monitoring and maintenance of complex in-service systems, Digital Twin technology has gained significant popularity over the past few decades. Digital Twins are virtual models of physical assets that enable real-time monitoring, control, and prediction of system behavior. A typical Digital Twin framework consists of five key components Kobayashi and Alam [2024a,b], Kobayashi et al. [2024a], Kabir and Alam [2010]: (1) a prediction module for real-time monitoring, (2) a real-time update module for synchronization, (3) data and signal processing, (4) visualization, and (5) decision-making modules. Within this framework, virtual sensors play a critical role in ensuring the performance and flexibility of the Digital Twin. These sensors continuously collect, analyze, and feed data into the digital twin in real time, supporting both the prediction and data processing components. When establishing digital twins Kobayashi et al. [2024b], virtual sensors can monitor and control physical sensors, offering cost-effective and scalable solutions. This is particularly useful in multi-criteria decision-making applications Martin et al. [2021], Kumar et al. [2022]. This capability allows the Digital Twin to maintain an accurate and reliable system representation, even when physical sensors degrade or experience faults. Ultimately, virtual sensors are essential to the scalability of Digital Twin technology, offering a cost-effective and adaptable solution for continuous real-time monitoring, informed decision-making, and system optimization in complex environments.

Emerging neural network technologies, such as the Deep Operator Network (DeepONet) Lu et al. [2021], Fourier Neural Operators (FNO) Li et al. [2020], and Physics-Informed Neural Networks (PINN) Raissi et al. [2019], provide powerful tools for developing virtual sensors that can predict the behavior of complex systems. These models are particularly adept at solving partial differential equations (PDEs) by approximating nonlinear operators and learning mappings between functional spaces. This makes them highly suitable for accurately modeling and predicting the behavior of complex systems with intricate interdependencies, such as those found in nuclear reactors. Among these, the Deep Operator Network (DeepONet) has demonstrated greater efficiency compared to the others. L. Lu, X. Meng and S. Cai *et al.* in their paper Lu et al. [2022] demonstrate that DeepONet is more flexible than FNO in terms of problem settings and datasets. With PINN as well, we face inconvenience as each new input parameter value requires a separate simulation or retraining. Moreover, PINN struggles to approximate PDEs with strong non-linearity commonly found in practical fluid flow problems. In contrast, DeepONet alleviates the need for retraining by learning operators that map entire functions, rather than specific input-output pairs, across different conditions. Once trained, DeepONet can generalize to a wide range of new inputs without requiring retraining for each new scenario, as it understands the underlying functional relationships between inputs and outputs. This is particularly advantageous for real-time applications, as it can handle varying conditions without the computational burden of frequent retraining. DeepONet approximates linear and nonlinear PDE solution operators using parametric functions as inputs and maps them to various PDE solution functions in output spaces, thereby eliminating the need for these repetitive training processes Koric and Abueidda [2023].

A well-trained neural operator offers the computational efficiency needed for real-time or near real-time predictions, which is crucial for control system optimization Kobayashi et al. [2024a], He et al. [2024]. These advantages make DeepONet our preferred choice for its flexibility, scalability, and efficiency. Unlike traditional finite element (FE) simulations, which can be computationally intensive and time-consuming, DeepONet can generate predictions orders of magnitude faster, making it ideal for real-time applications. By training on data from high-fidelity simulations and experimental measurements, DeepONet can accurately predict coolant flow behavior under various operating conditions, which is central to our goal of developing an effective virtual sensor framework for nuclear reactors. The key advantage of using DeepONet for our problem is its trunk network, which processes spatial coordinates to evaluate the output function Lu et al. [2021], He et al. [2024]. This network enables us to predict parameters at various points along the pipe based on input data from a single location, allowing for comprehensive condition inference throughout the entire pipe from just one input plane. Combined with near real-time computational ability, DeepONet acts effectively as virtual sensors, providing real-time estimates of flow velocity, turbulence, pressure, and temperature at various points in the primary circuit without physical sensors. Thus, the application of DeepONet offers a solution to many of the challenges posed by current methods for monitoring coolant flow in nuclear reactors.

In this work we have studied hot leg as the representation of primary coolant system to demonstrate the effectiveness of DeepONet in predicting the parameters. The hot leg, comprising horizontal and vertical conduits along with elbows, transports highly pressurized, high-temperature water from the reactor pressure vessel (RPV) to the steam generator (SG). Any leakage in the hot leg can lead to serious consequences, including a loss of coolant accident (LOCA), which may impair the reactor's cooling capacity and pose radiological risks. Thus, it is beneficial to monitor the coolant condition inside the hot leg to ensure proper heat transfer and safe, efficient operation of reactor. However, real time monitoring of key parameters like pressure, velocity, and turbulence kinetic energy inside the hot leg poses challenges due to its critical operating conditions. We aim to develop a real-time monitoring model of thermal-hydraulic conditions within the hot leg of PWR. We have specifically considered the coolant system of AP1000 shown in Figure 1. For this study, we propose to utilize the coolant inlet velocity, which is already monitored through existing sensor networks. We assume that the coolant flow through the hot leg follows the normal operational conditions of a PWR coolant system.

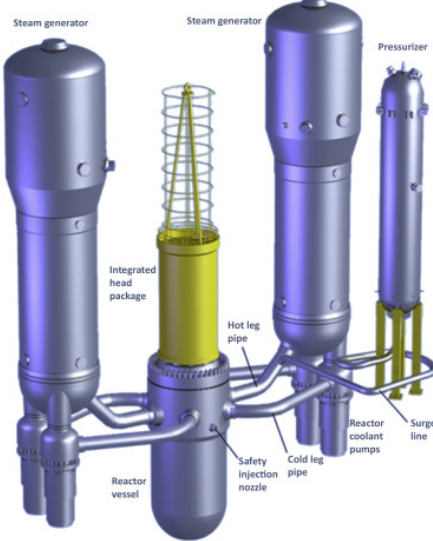


Figure 1: Schematic diagram of AP-1000 reactor coolant system Namgung and Giang [2016a].

Based on this information, we aim to develop a model that predicts specific thermal-hydraulic parameters (pressure, velocity, and turbulence kinetic energy) in the central plane of the hot leg. Monitoring these parameters is important not only for understanding the overall heat transfer performance but also for ensuring the structural integrity of the piping system. High or fluctuating pressure can exert mechanical stress on the piping material, leading to issues such as wear, fatigue, and cracking. Sudden pressure drops may also signal blockages or leaks, which could further accelerate degradation. Monitoring velocity is equally important, as high coolant flow speeds, particularly in areas where the flow direction changes, can induce flow-induced vibrations, leading to mechanical fatigue and increasing the risk of erosion and corrosion. In turn, these conditions can thin the pipe walls over time. Turbulence, especially near bends and joints, amplifies stress on the piping structure, contributing to fatigue and accelerating the erosion-corrosion process. It also introduces hydraulic shocks and uneven temperature distributions, which weaken material integrity over time. Given the critical role that pressure, velocity, and turbulence play in the degradation of piping material, our goal is to develop a real-time monitoring model of the thermal-hydraulic conditions within the hot leg of a PWR.

The key contribution of our work is demonstrating the feasibility and benefits of using DeepONet for real-time monitoring of coolant flow in the primary circuit of a nuclear reactor. Our study highlights the potential of virtual sensors to significantly improve the monitoring and inspection of reactor components. Through comprehensive simulations and experimental validation, we show how this approach delivers highly accurate and timely data, facilitating proactive maintenance and optimizing reactor operations.

2 Methods

2.1 Data Generation

The hot leg in an AP1000 reactor plays a critical role in its operation, acting as the primary channel for transferring heat generated in the reactor core to the steam generators. Hence, the core could overheat without proper flow through the hot leg, leading to a potential meltdown. AP1000 reactor cooling system includes hot and cold leg pipes connecting the reactor vessel, steam generators, and reactor coolant pumps. Each loop has three pipes, including a 787.4 mm inner diameter pipe between the reactor vessel outlet and steam generator inlet with a length of 2.3 m Namgung and Giang [2016b]. While system-level codes provide a useful tool for macroscopic thermal-hydraulic analysis of nuclear reactors, their limitations in resolving detailed flow features such as flow re-circulation and turbulence within the hot leg necessitate the use of more advanced methods like Computational Fluid Dynamics (CFD). CFD, with its ability to resolve complex geometries and flow physics, can provide a more accurate and detailed understanding of the fluid dynamics within the hot leg. However, due to the complexity of the full-scale geometry, a scaled-down model was used for CFD analysis. Geometric scaling was employed, ensuring a constant flow rate per unit volume between the actual case and the model. In this study, geometric scaling was implemented according to the following conditions:

$$\frac{Q_m}{V_m} = \frac{Q_a}{V_a}$$

Where, Q_m and Q_a are the volumetric flow rates of model and actual case and V_m V_a are the volume which results in volume of the model and actual case. Hence we can write,

$$\frac{v_m}{v_a} = \frac{l_m}{l_a}$$

where v_m and the v_a are the velocities of the model and the actual case. l_m and l_a represents the model and actual flow length the hot leg. The diameter of the hotleg pipe (d_a) was scaled down by a factor of λ equivalent to 31.5 which gives the value of d_m to be 25 mm. The flow length of the model was kept 150 mm where $l_a = d_m \times l_m$. Hence, the relationship between the Reynolds number (Re) for the model and actual scenario becomes:

$$Re_m = Re_a \times \frac{\lambda}{d_m}$$

As shown in Figure 2, the elbow joint angle (θ_c) was kept 120° , same as the actual scenario of hot leg.

The walls of the flow domain were treated as adiabatic and subject to no-slip conditions. This implies that these surfaces neither gained nor lost heat, and fluid velocity at the wall interface was zero. In terms of thermal conditions, the inlet fluid temperature was maintained at 594.3 K. The outlet was set to a gauge pressure of zero, ensuring it remained at ambient atmospheric pressure. The inlet velocity (v_{in}) was changed according to the magnitude of Re, ensuring turbulent flow. Figure 2 shows the essential boundary conditions and the plane of interest where the hydrodynamics parameters evaluated through CFD simulations to train ML model.

In the numerical investigations, the coolant was modeled as a Newtonian fluid with constant viscosity and density, implying a linear relationship between stress rate and strain rate. Simulations were performed under steady-state conditions, encompassing both forced turbulent flow regimes. 3D Navier-Stokes equations solved using the Finite Volume Method (FVM). The governing equations are as follows Ahmed et al. [2024]:

Continuity equation:

$$\frac{\partial \rho}{\partial t} + \nabla \cdot (\rho \vec{v}) = 0$$

Momentum equation:

$$\frac{\partial (\rho \vec{v})}{\partial t} + \nabla \cdot \rho \vec{v} \vec{v} = -\nabla P + \nabla \bar{\tau} + \rho g$$

Energy equation:

$$\frac{\partial (\rho H)}{\partial t} + \nabla \cdot (\rho H \vec{v}) = -\nabla \cdot \vec{q}'' + q''' - P \nabla \cdot \vec{v}$$

In the present study, forced turbulent flows were assessed employing the RNG $k - \varepsilon$ model, the equations for which are presented below Ahmed et al. [2022, 2021]:

$$\begin{aligned} \frac{\partial}{\partial t} (\rho k) + \frac{\partial y}{\partial z_i} (\rho \varepsilon u_i) &= \frac{\partial}{\partial z_j} \left(\alpha_k \mu_{\text{eff}} \frac{\partial k}{\partial z_j} \right) + G_k + G_b - \rho \varepsilon - Y_M + S_k \\ \frac{\partial}{\partial t} (\rho \varepsilon) + \frac{\partial y}{\partial x_i} (\rho \varepsilon u_i) &= \frac{\partial}{\partial z_j} \left(\alpha_k \mu_{\text{eff}} \frac{\partial k}{\partial z_j} \right) + C_{1\varepsilon} \frac{\varepsilon}{k} (G_k + C_{3k} G_b) - C_{2\varepsilon} \rho \frac{\varepsilon^2}{k} - R_\varepsilon + S_\varepsilon \end{aligned}$$

In the FVM, the establishment of a computational grid over the geometry is essential for attaining solution convergence. To facilitate this, the present study employed hexahedral and tetrahedral mesh spanning the entire computational domain, with particular attention dedicated to enhanced wall treatment for improved accuracy. Mesh with refined wall treatment, including ten boundary layers, was employed to ensure solution convergence. Mesh elements were finely sized at

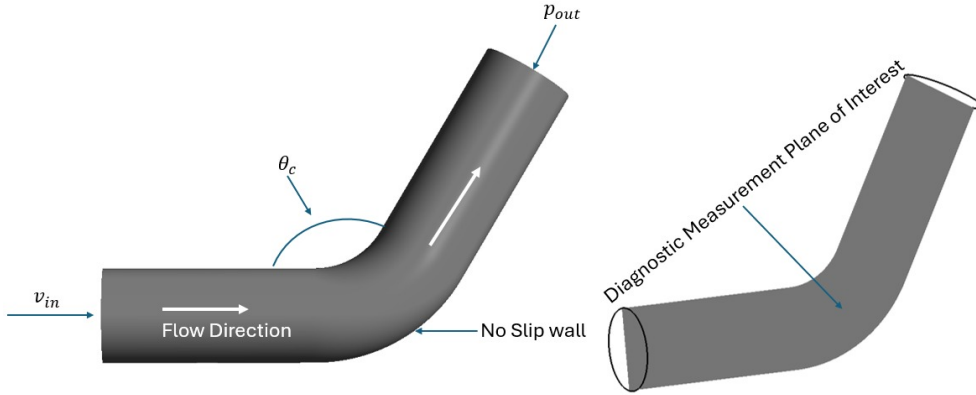


Figure 2: Computational domain and boundary conditions

3.75 mm near critical regions. Mesh quality metrics were strictly controlled, with skewness and orthogonal quality maintained at 0.11 and 0.96, respectively, across all channel configurations. Figure 3 represents the grid generation over the fluid domain.

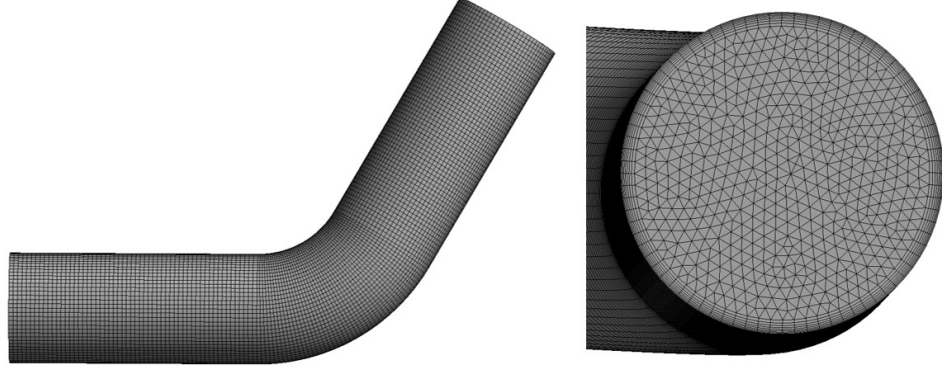


Figure 3: Grid generation over the domain

This study utilized an implicit time-marching scheme to solve the governing equations. The pressure-velocity coupling was achieved through the SIMPLEC algorithm. For the discretization of mass, momentum, and energy conservation equations, a second-order upwind scheme was implemented, balancing accuracy and computational efficiency. The turbulence kinetic energy and dissipation rate equations were discretized using a first-order upwind scheme, chosen for its robustness and stability in turbulent flow simulations. The turbulence intensity (I) at the inlet was specified based on the following empirical relationship Homicz [2004]:

$$I \equiv \frac{\sqrt{\frac{2}{3}k}}{U_{\text{avg}}} \approx \frac{0.16}{Re^{1/8}}$$

2.2 DeepONet

In this study we have used an unstacked DeepONet described by Lu Lu *et al.* Lu et al. [2021], comprising a single branch network and a trunk network. Figure 4 shows the model architecture used in this work. DeepONet architecture provides a foundation for capturing the interplay between input parameters and spatial coordinates. The branch network processes the input function, representing the average initial velocity in our case. This input, belonging to an infinite-dimensional functional space, is characterized by n control points. Here $n=1$ as we are considering the average value. The trunk

network, on the other hand, handles the spatial information. It takes as input a collection of N points within the domain, each defined by its (x, y, z) coordinates. In our study, these points correspond to 11340 virtual sensors ($N=11340$) distributed throughout the pipe section. The trunk network encodes the spatial dependencies inherent in the problem.

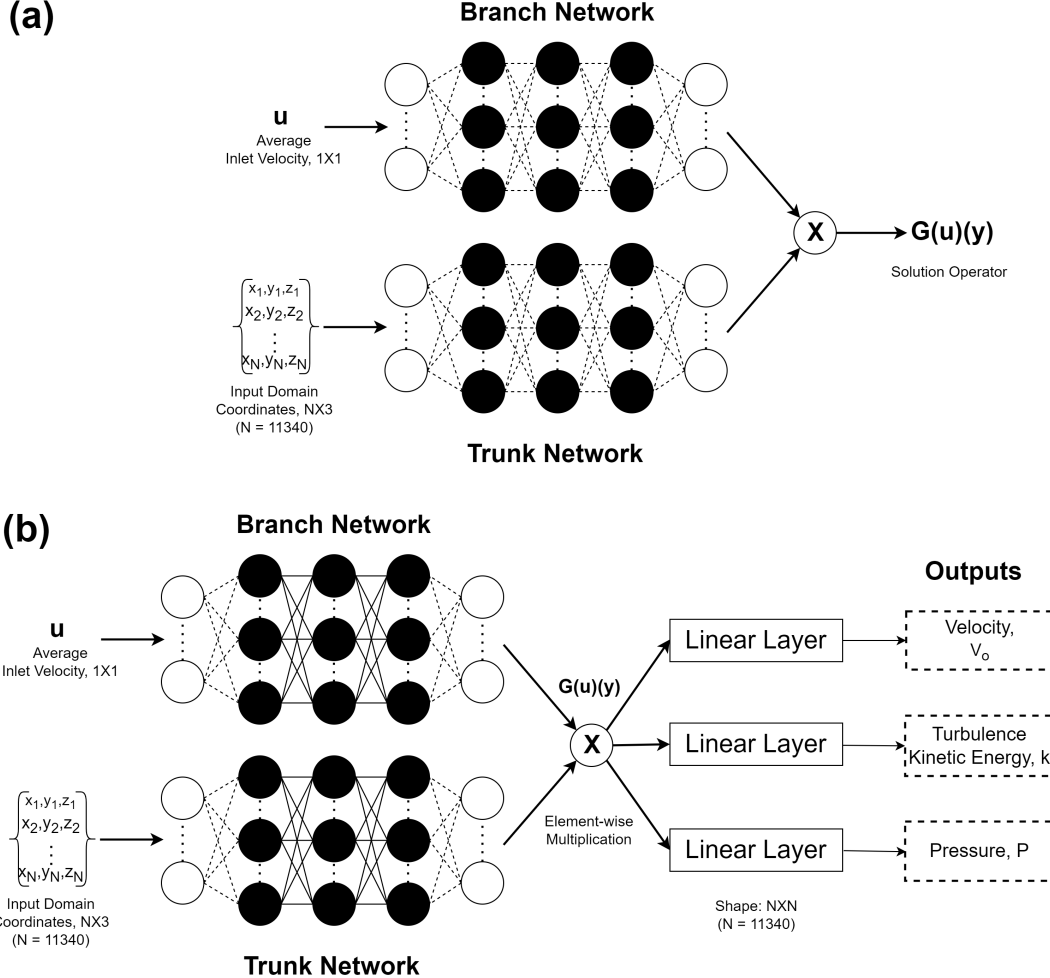


Figure 4: Schematic of the FNN-based DeepONet architecture used in this study. The model consists of a single branch and trunk network. The branch network takes the average inlet velocity (u) as input, and the trunk network takes the spatial domain coordinates (x, y, z). The output quantities are distributions of coolant pressure (P), velocity (V_o), and turbulence kinetic energy (k). The schematic (a) shows the original DeepONet architecture. The Branch network has 11 hidden layers and the trunk network has 10 hidden layers with 4096 neurons each. (b) The schematic illustrates the modified architecture with additional linear layers for each parameter. The branch network has layer sizes of $[n, 512, 512, 512, N]$ where $n = 1$, and the trunk network has layer sizes of $[3, 512, 512, 256, 3]$, both utilizing ReLU activation. At the end, there are three linear layers, each with sizes $[N, N]$, where $N = 11,340$, without any activation.

The crux of the DeepONet lies in the fusion of information from the branch and trunk networks. This integration is achieved through element-wise multiplication Jin et al. [2022], He et al. [2023] of the outputs from Branch and Trunk Networks. The resulting output, $G(u)(y)$, is a function of the spatial coordinates y conditioned on the input function u . This formulation empowers the network to learn complex mappings between input and output spaces. To enhance the model's predictive capabilities, we incorporated additional linear layers into the original DeepONet architecture. These layers enable scaling and shifting of the output, improving alignment with the target values. Figure 4 displays the original model architecture introduced by Lu Lu *et al.* Lu et al. [2021] alongside the modified architecture used in this study. The concept of utilizing linear layers was inspired by Kazuma *et al.* ? In the results section, we present a comparison between the models with and without the additional linear layers to further justify our modifications. The DeepONet model was trained to predict three primary output functions: turbulence, pressure, and velocity distributions in the central plane of the hot leg. These output functions reside in distinct functional spaces, denoted as S_1 , S_2 , and S_3 ,

where $k \in S_1$, $p \in S_2$, and $v_o \in S_3$ represent turbulence, pressure, and velocity values in the central plane. And the mapping solution operators of the DeepONet can be defined as G_1 , G_2 and G_3 for three different parameters.

For both branch and trunk networks, we employed Feedforward Neural Networks (FNNs) due to their simplicity and effectiveness in approximating nonlinear functions. The architecture of these FNNs included three hidden layers, with the number of neurons in each layer determined through hyperparameter tuning. This hyperparameter optimization process was crucial in achieving optimal performance. The activation function of choice for the branch and trunk networks was the Rectified Linear Unit (ReLU). The Adam optimizer, known for its efficiency and stability, was employed to update the network parameters iteratively. The training process involved minimizing the scaled Mean Squared Error (MSE) loss function:

$$\text{MSE Loss} = \frac{1}{N} \sum_{i=1}^N (y_i - \hat{y}_i)^2 \quad (1)$$

where N presents the number of data points (no of nodes), y_i is the predicted value, and \hat{y}_i is the true value.

3 Results and Discussion

3.1 Data Processing

The data for this study was generated using ANSYS Fluent, focusing on fluid dynamics within the hot leg elbow joint of an AP-1000 LWR nuclear reactor. The average inlet velocity range for the simulations was set between 0.63 and 0.83. The computational mesh consisted of a total of 11,340 nodes, distributed along the central plane of the hot leg to capture the coolant flow characteristics throughout the pipe section. For this study, we performed a total of 5,000 simulations. This dataset was subsequently divided into a training and testing set in a 90%-10% ratio, resulting in 4,500 scenarios for training and 500 scenarios for testing. Importantly, the 500 test data points were never touched during the training or validation process. They remained completely unseen by the model and were used exclusively at the final stage to evaluate the model's performance on unseen data. This setup was designed to monitor coolant behavior in near-real-time, capturing detailed velocity, turbulence, and pressure variations to detect any anomalies effectively.

To ensure the DeepONet model properly learns the values of different parameters, we addressed the issue of varying ranges among these parameters. For instance, the pressure values range between approximately -231.25 and 132.7, while the turbulence kinetic energy values range between approximately 0.000875 and 0.019015. Such discrepancies in value ranges can hinder the model's learning process. To mitigate this difference, we applied min-max scaling to normalize all the values between 0 and 1.

$$X_{\text{scaled}} = \frac{X - X_{\min}}{X_{\max} - X_{\min}} \quad (2)$$

where X is the original value, X_{\min} is the minimum value in the dataset, X_{\max} is the maximum value in the dataset, and X_{scaled} is the normalized value in the range $[0, 1]$.

Figure 5 provides a visual representation of this scaling process. The histograms in the top row display the original values of kinetic turbulence energy, pressure, and velocity. The bottom row shows the scaled values of these parameters after applying min-max scaling. From these histograms, it is evident that the original values of turbulence (a), pressure (b), and velocity (c) are distributed across different ranges. The original turbulence values are densely packed near the lower end of the range, with a significant peak around 0.0025. The pressure values exhibit a broader distribution with notable peaks around -50 and 50. The velocity values are concentrated between 0.6 and 0.8, with a pronounced peak near 0.75. After scaling, the turbulence values (d) are now spread across the $[0, 1]$ range, maintaining the original distribution shape but normalized. The scaled pressure (e) and velocity (f) values are also within the range of $[0, 1]$, preserving the distribution characteristics seen in the original data. By scaling these parameters, we ensure that the DeepONet model can learn effectively from the data, with each parameter contributing proportionately to the training process. This step helps improving the model's accuracy and reliability in predicting coolant behavior.

3.2 Training Process

The training process for this study is designed to ensure that the model fits the training data well while also generalizing effectively to unseen data. Initially, the training dataset is split into two parts: 80% for training and 20% for validation.

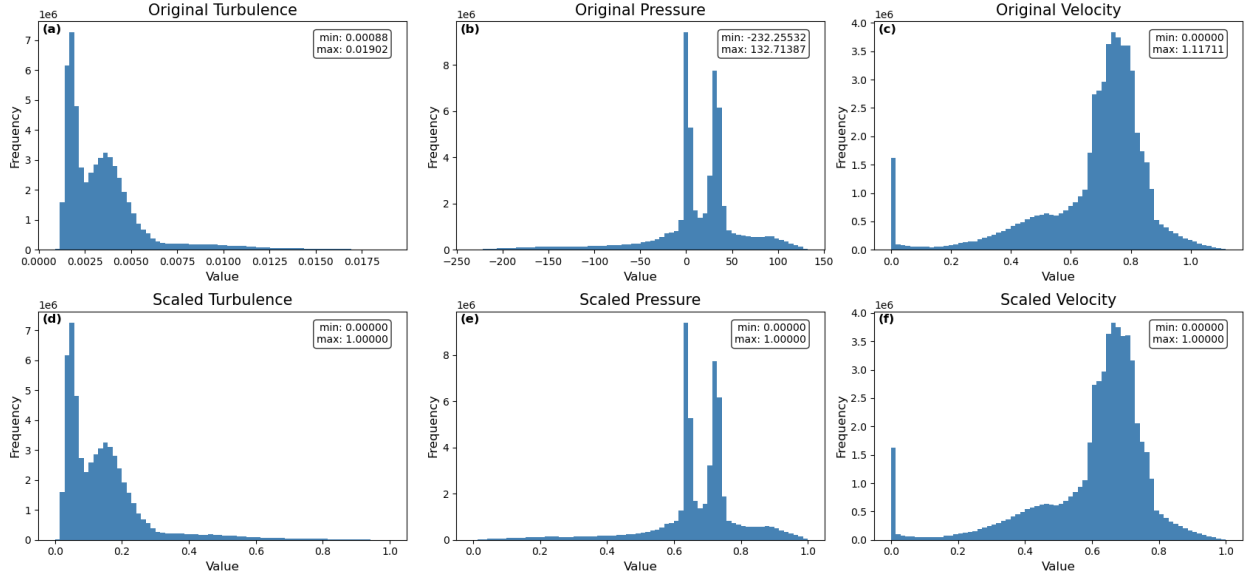


Figure 5: Histograms of original and scaled parameter values. The top row displays the original values for turbulence, pressure, and velocity, showing distinct distributions. The bottom row presents the values after min-max scaling, normalizing all parameters to the $[0,1]$ range.

The model was trained for 100 epochs to ensure convergence with this specific dataset, activation function, and optimizer. The number of hidden layers for the model was fixed at three, but the number of neurons in each layer was determined through hyperparameter tuning.

Hyperparameter tuning was achieved through Bayesian optimization using the Optuna framework, which efficiently searches for optimal parameters. The loss function employed was Mean Squared Error (MSE), and the model was optimized using the Adam optimizer with L2 regularization to prevent overfitting. Training was conducted over 100 epochs, with early stopping implemented to halt training if performance did not improve within 5 consecutive epochs, ensuring efficient use of computational resources. The model undergoes 5-fold cross-validation to assess its generalization capabilities across different subsets of the dataset. This process ensures that each data point is used for both training and validation, providing a comprehensive evaluation of the model's performance. The average performance across all five folds gives a reliable estimate of how well the model will generalize to new data. The total training duration was 19 hours and 38 minutes. The computations for the training and evaluation tasks were performed on a computational node with a single NVIDIA A100 GPU within the Delta cluster hosted by the National Center for Supercomputing Applications (NCSA). The hyperparameter tuning process for the DeepONet neural networks involved an extensive search to identify the optimal configuration using Bayesian optimization with the Optuna framework. Table 1 summarizes the ranges and best values found for each parameter.

Table 1: Summary of Hyperparameter Tuning for DeepONet.

Parameter Tuned	Range	Best Value Found
No of Neurons for each hidden layer	128, 256, 512	512
Dropout Rate	0.0 to 0.3	0.0013836
Learning Rate	10^{-5} to 10^{-3}	0.00098
Batch Size	16, 32, 64	16
Weight Decay Rate	10^{-8} to 10^{-6}	1.53625e-08
Number of Trials	50	NAN

After confirming that the model generalizes well through cross-validation, the next step is to train the model on the entire dataset for an extended period of 1000 epochs. For this final training phase, the hidden layer configuration was $[512, 512, 512]$, the dropout rate was set to 0.0, the weight decay rate was 10^{-8} , and the learning rate was 0.001. Training on the whole dataset allows the model to learn from all available data, maximizing its potential to capture complex patterns. The extended training period ensures that the model has sufficient time to converge to an optimal solution.

After training the model on the entire dataset, the best model is then used to make predictions on the test dataset. The test dataset consists of data points that were not used during training or validation, providing an unbiased evaluation of the model’s performance. These 500 test data points remained completely unseen by the model and were used exclusively at this stage to evaluate the model’s performance on unseen data. To evaluate the model on test dataset following quantities were calculated:

$$\text{Mean Square Error (MSE)} = \frac{1}{N} \sum_{i=1}^N (y_i - \hat{y}_i)^2 \quad (3)$$

$$\text{Mean Absolute Error (MAE)} = \frac{1}{N} \sum_{i=1}^N |y_i - \hat{y}_i| \quad (4)$$

$$\text{Relative L2 Error} = \frac{\|y_i - \hat{y}_i\|_2}{\|y_i\|_2} \quad (5)$$

where y_i represents the true values generated through finite element method, \hat{y}_i represents the predicted values from neural network, and N is the total number of data points.

3.3 Vanilla DeepONet vs DeepONet with Linear Layers

To support our modification of the original model with added linear layers for each parameter separately, we present a comparison between the DeepONet model with and without these linear layers. To match the total number of learnable parameters for both of the model, the number of hidden layers for Vanilla DeepONet model was taken to be 11 for Branch network and 10 for Trunk network. Each hidden layer has 4096 neurons. Which makes the total number of learnable parameters to be 365431887. On the other hand, our considered model with linear layer has 3 hidden layers with 512 neurons each. With the extra three linear layers at the end, the total number of learnable parameters for this model is 361499727. With that these two models become comparable with each other. Table 2 shows the average value, standard deviation, and maximum value of the mean square error (MSE) and relative L2 error on the test dataset for each model, evaluated separately for the three parameters: pressure, velocity and turbulence kinetic energy.

Parameters	Model	Mean Square Error (MSE)		Relative L2 Error	
		Average (Std)	Maximum Value	Average (Std)	Maximum Value
Pressure (P)	Original DeepONet	$5.00 \times 10^{-4} (2.30 \times 10^{-4})$	1.02×10^{-3}	$3.17 \times 10^{-2} (7.37 \times 10^{-3})$	4.68×10^{-2}
	With Linear Layers	$2.60 \times 10^{-4} (2.30 \times 10^{-4})$	8.80×10^{-4}	$2.01 \times 10^{-2} (1.18 \times 10^{-2})$	4.28×10^{-2}
Velocity (V_o)	Original DeepONet	$4.02 \times 10^{-3} (1.52 \times 10^{-3})$	8.31×10^{-3}	$1.00 \times 10^{-1} (2.30 \times 10^{-2})$	1.61×10^{-1}
	With Linear Layers	$1.40 \times 10^{-3} (1.27 \times 10^{-3})$	4.59×10^{-3}	$5.14 \times 10^{-2} (3.01 \times 10^{-2})$	1.09×10^{-1}
Turbulence Kinetic Energy (k)	Original DeepONet	$1.46 \times 10^{-3} (5.20 \times 10^{-4})$	2.96×10^{-3}	$1.95 \times 10^{-1} (3.30 \times 10^{-2})$	2.84×10^{-1}
	With Linear Layers	$5.30 \times 10^{-4} (4.80 \times 10^{-4})$	1.81×10^{-3}	$1.03 \times 10^{-1} (6.05 \times 10^{-2})$	2.33×10^{-1}

Table 2: Comparison of Mean Square Error (MSE) and Relative L2 Error for Original DeepONet and DeepONet with additional Linear Layers.

Analyzing the data in Table 2, it is evident that the model with linear layers consistently outperforms the original DeepONet model across all parameters. For pressure (P), the MSE average decreases from 0.00048 to 0.00026, and the relative L2 error average drops from 0.03106 to 0.0204, indicating a significant improvement in predictive accuracy. Similarly, for velocity (V_o), the model with linear layers shows a reduction in the MSE average from 0.00281 to 0.00141, and a decrease in the relative L2 error average from 0.07934 to 0.05184. Turbulence kinetic energy (k) also benefits from the linear layers, with the MSE average reducing from 0.00105 to 0.00054, and the relative L2 error average declining from 0.15924 to 0.10573. These enhancements demonstrate the efficacy of the added linear layers in refining the model’s alignment with target values, thus validating our modifications.

3.4 Impact of Data Splits and Node Counts on Model Accuracy

To evaluate the impact of different train-test splits on the model’s performance, the dataset was divided into the following ratios: 70-30%, 80-20%, and 90-10%. The model was trained on these varying fractions of the training set, and the

average Mean Squared Error (MSE) and Relative L2 error were calculated for each test split. It was hypothesized that the model's performance would degrade with a smaller training dataset, as less data typically leads to poorer model performance. However, the results were surprisingly consistent across different splits, as shown in Table 3.

Train-Test Split	Average MSE			Average Relative L2 Error		
	Pressure	Velocity	Turbulence	Pressure	Velocity	Turbulence
90%-10%	2.59×10^{-4}	1.41×10^{-3}	5.39×10^{-4}	2.04×10^{-2}	5.18×10^{-2}	1.06×10^{-1}
80%-20%	2.55×10^{-4}	1.40×10^{-3}	5.28×10^{-4}	2.01×10^{-2}	5.13×10^{-2}	1.03×10^{-1}
70%-30%	2.58×10^{-4}	1.42×10^{-3}	5.37×10^{-4}	2.04×10^{-2}	5.22×10^{-2}	1.07×10^{-1}

Table 3: Average MSE and Relative L2 error for different train-test splits.

As seen in Table 3, the performance metrics (MSE and Relative L2 error) for pressure, velocity, and turbulence remain very close across different training data fractions. This consistent performance across various training sizes demonstrates that the model is inherently robust, capable of achieving high performance even with varying amounts of training data. The model has effectively learned the underlying patterns of the dataset, ensuring reliable predictions. Each of the training datasets, from 70% to 90%, contains enough data for the model to generalize well, thus explaining the minimal performance differences. The model's effective regularization techniques prevent overfitting, ensuring stable performance across different training sizes. These findings confirm that the model has been trained with a sufficient amount of data and performs well even with reduced training data. This robust performance implies that the model can be effectively used in scenarios with limited data availability. Moreover, the ability to maintain accuracy with varying training sizes indicates that the model is versatile and reliable. For the rest of the studies and demonstrations, we have chosen the 80-20 train-test split as it is a standard practice in the field, providing a good balance between training and testing data.

In a separate experiment, the train-test split was kept constant at 80%-20% while varying the number of nodes used for training. The original number of nodes was 11,340, and this was compared to a reduced number of 2,835 nodes which is one forth of the original number. The results, presented in Table 4, show that the model provided consistent performance even when the number of nodes was reduced by three-fourths.

Number of Nodes	Average MSE			Average Relative L2 Error		
	Pressure	Velocity	Turbulence	Pressure	Velocity	Turbulence
11340	2.55×10^{-4}	1.40×10^{-3}	5.28×10^{-4}	2.01×10^{-2}	5.13×10^{-2}	1.03×10^{-1}
2835	2.68×10^{-4}	1.42×10^{-3}	5.07×10^{-4}	2.07×10^{-2}	5.14×10^{-2}	1.03×10^{-1}

Table 4: Average MSE and Relative L2 error for different numbers of nodes.

As shown in Table 4, the performance metrics (MSE and Relative L2 error) for pressure, velocity, and turbulence remain consistent across the different numbers of nodes. This suggests that the model's performance is not heavily dependent on the number of nodes used for training, indicating that the model is capable of maintaining accuracy even with fewer nodes. This robustness implies that the model can be effectively scaled down, which can be advantageous for computational efficiency without sacrificing predictive accuracy.

These two experiments demonstrate the consistency of the model's performance across varying training data sizes and different numbers of nodes, indicating its potential reliability in diverse scenarios. These findings highlight that the model is well-trained with the available data and can still perform effectively even with smaller datasets, making it practical for various applications and computationally efficient.

3.5 Performance Evaluation

Building on our previous studies—comparing Vanilla DeepONet to DeepONet with Linear Layers, and analyzing the impact of data splits and node counts on model accuracy—we now focus on a comprehensive analysis of the modified DeepONet with linear layers using an 80-20 train-test split. This section provides a comprehensive evaluation of the model's performance across the key parameters of turbulence kinetic energy, velocity, and pressure. Table 5 summarizes the average Mean Absolute Error (MAE), Mean Squared Error (MSE), and Relative L2 error for the individual parameters on the test dataset. The results indicate that the model performs best in predicting pressure, as evidenced by the lowest values in MSE, MAE, and Relative L2 error. In contrast, while the MSE and MAE for

velocity and turbulence remain relatively small, the model shows higher errors for velocity. Turbulence exhibits the worst performance in terms of Relative L2 error, with a relative error of 10.58%.

Table 5: Average MAE, MSE, and Relative L2 error for individual parameters on the test dataset.

Parameters	MSE	MAE	Relative L2 Error
Velocity	1.401×10^{-3}	3.1264×10^{-2}	5.1348×10^{-2}
Pressure	2.550×10^{-4}	8.714×10^{-3}	2.0108×10^{-2}
Turbulence	5.280×10^{-4}	1.6848×10^{-2}	1.03441×10^{-1}

To further illustrate the model’s performance, we provide a detailed error distribution analysis using histograms in Figure 6. These histograms help us better understand the frequency distribution of MSE and Relative L2 error across the test dataset for each parameter, offering deeper insight into the variability and consistency of the model’s predictions. Panel (a) presents the distribution of MSE values for pressure predictions, indicating a concentration of lower error values, which suggests a strong model performance in pressure estimation. Similarly, panel (c) shows the model’s MSE distribution for velocity predictions, and panel (e) for the turbulence kinetic energy. The right-hand panels, (b), (d), and (f), illustrate the relative L2 error percentages. The embedded statistics within these panels (mean, standard deviation, and quantiles) summarize the error distribution, offering a comprehensive perspective on the model’s performance.

The histograms for pressure predictions (Panels (a) and (b)) show a concentration of lower error values, indicating a strong and consistent model performance in estimating pressure. The narrow spread of MSE and Relative L2 error values reflects the model’s ability to make accurate and reliable pressure predictions with minimal variability. For velocity predictions (Panels (c) and (d)), the MSE values exhibit a larger spread, suggesting greater variability in the model’s accuracy for this parameter. The higher MSE for velocity indicates that, on average, the errors in velocity predictions are larger compared to those in pressure predictions. However, the Relative L2 error for velocity is lower than that for turbulence, which means that, relative to the magnitude of the true values, the errors in velocity predictions are smaller compared to the errors in turbulence predictions. Turbulence kinetic energy predictions (Panels (e) and (f)) present the most significant challenge for the model. Although the MSE for turbulence is lower than that for velocity, the Relative L2 error is higher. This discrepancy signifies that while the mean square error in turbulence predictions might be smaller, the error relative to the actual values of turbulence is larger. In other words, the model’s errors in predicting turbulence are more significant when viewed in the context of the scale of the turbulence values. This high Relative L2 error indicates that the model struggles more with predicting turbulence accurately compared to velocity and pressure, reflecting the complex nature of turbulence and the inherent difficulty in modeling it accurately.

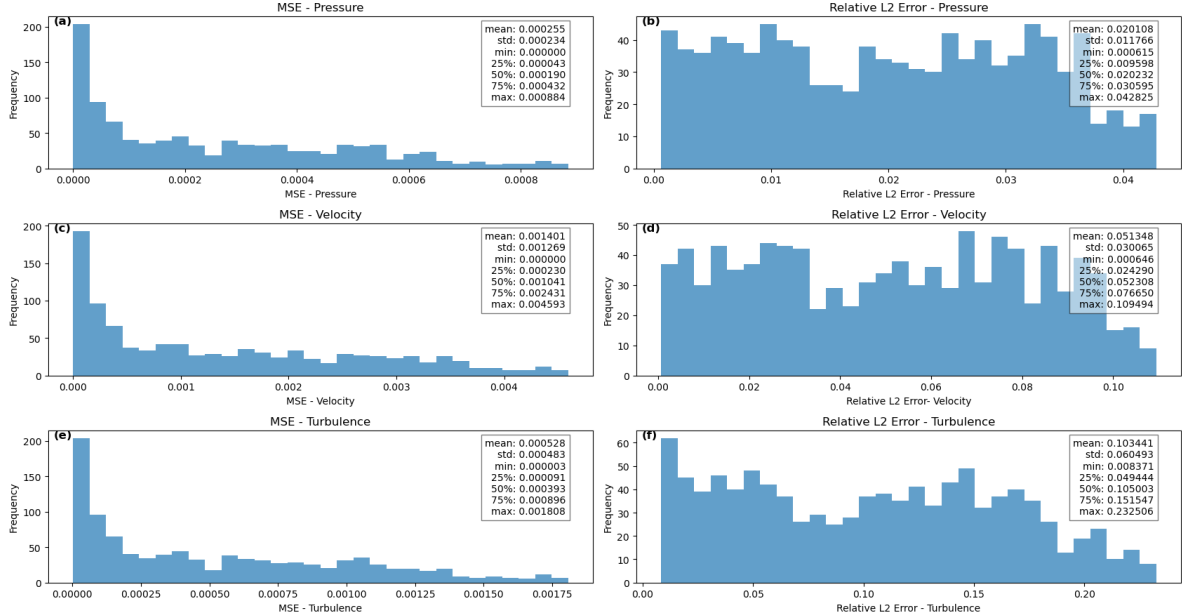


Figure 6: Distribution of model performance metrics for DeepONet on the test dataset.

To gain a deeper understanding of the model’s predictive performance, particularly in identifying which parameters are predicted poorly and which parts of the data the model struggles with, we will include a detailed visual representation

in Figure 7, 8 and 9. This figure will showcase the FEM simulated data, the neural network’s predictions, and the corresponding errors. To provide a comprehensive analysis, we have included five different plots for each parameter—pressure, velocity, and turbulence kinetic energy. These plots illustrate the best-case scenario, the worst-case scenario, and the transitional states between these extremes. By examining these visualizations, we can pinpoint the specific regions within the pipe where the model encounters difficulties in accurately predicting the coolant behavior. The best-case scenario plots highlight instances where the model’s predictions closely match the FEM simulated data, showcasing optimal performance. In contrast, the worst-case scenario plots reveal significant prediction errors with the highest discrepancies. The intermediate plots illustrate the gradual transition between these extremes, offering insights into how and where the model’s performance deteriorates. This detailed visual analysis will not only help us understand which parameters the model predicts poorly but also identify the specific sections of the pipe where these inaccuracies occur. By doing so, we can gain valuable insights into the model’s limitations and areas that require further refinement to improve the overall accuracy and reliability of the predictions.

3.6 Inference Time

DeepONet is well-known for its short inference time, especially when compared to traditional numerical methods such as the Finite Element Method (FEM). After the model has been fully trained, a well trained DeepONet model can generate predictions almost instantaneously for new inputs. This is because it bypasses the need for iterative solving of differential equations, which is computationally expensive in traditional methods like FEM.

	FE Simulation Time [s]	Inference Time [s]
FE Simulation	200	-
DeepONet	-	1.2×10^{-3}

Table 6: Comparison of inference time between DeepONet and FEM

Table 6 shows the inference time for DeepONet in comparison to FE simulation. As we can see, DeepONet is approximately 166,000 times faster than FEM, which requires 200 seconds for a single simulation. This drastic reduction in prediction time makes DeepONet particularly useful for virtual sensing. This further reinforces our choice of utilizing DeepONet for this study.

3.7 Local Variable Analysis and Discussion

Figure 7 presents the velocity contours for both the true and predicted values, along with the associated error distribution, on a selected diagnostic plane. The figure showcases the results for five representative cases, ranging from the best-performing case to the worst-performing case, with the intermediate cases illustrating a 25% interval distribution of best performing case. The figure demonstrates that DeepONet, while generally proficient at predicting velocity patterns, encounters difficulties in regions with abrupt velocity transitions, particularly near the elbow joint where steep gradients and discontinuities are prevalent due to flow separation from the inner radius. In these areas, the model exhibits higher prediction errors compared to regions with smoother flow fields. This discrepancy can be attributed to the inherent challenge of capturing sharp gradients and discontinuities using a data-driven model like DeepONet. While the flow behavior in these zones is governed by intricate physical laws, DeepONet primarily relies on learning patterns from training data. Consequently, the model struggles to achieve high accuracy in regions where the flow physics plays a dominant role. This limitation is consistently observed across all five cases presented.

Analysis of Turbulence Kinetic Energy (TKE) in Figure 8 reveals that DeepONet accurately predicts turbulence patterns. However, error patterns for TKE are inversely related to those observed in velocity predictions. TKE magnitude increases downstream of the elbow due to flow separation and recirculation, resulting in pressure gradients and upsurged the turbulence. DeepONet excels at predicting local zones with high TKE values, but accuracy diminishes in regions of low TKE, even with smooth flow fields. This could be attributed to the nature of TKE magnitudes, which are near zero in smooth flows and significantly higher in turbulent regions. DeepONet struggles to capture these subtle variations near zero, leading to the observed error pattern reversal compared to velocity fields. Furthermore, the contour plots reveal instances of exceptionally high errors at specific nodes within the diagnostic plane, suggesting the presence of outliers in the predicted data. These outliers, characterized by significant deviations from the true values, could arise from various factors such as noise in the training data, model limitations in handling extreme or rare flow conditions, or numerical instabilities during the prediction process.

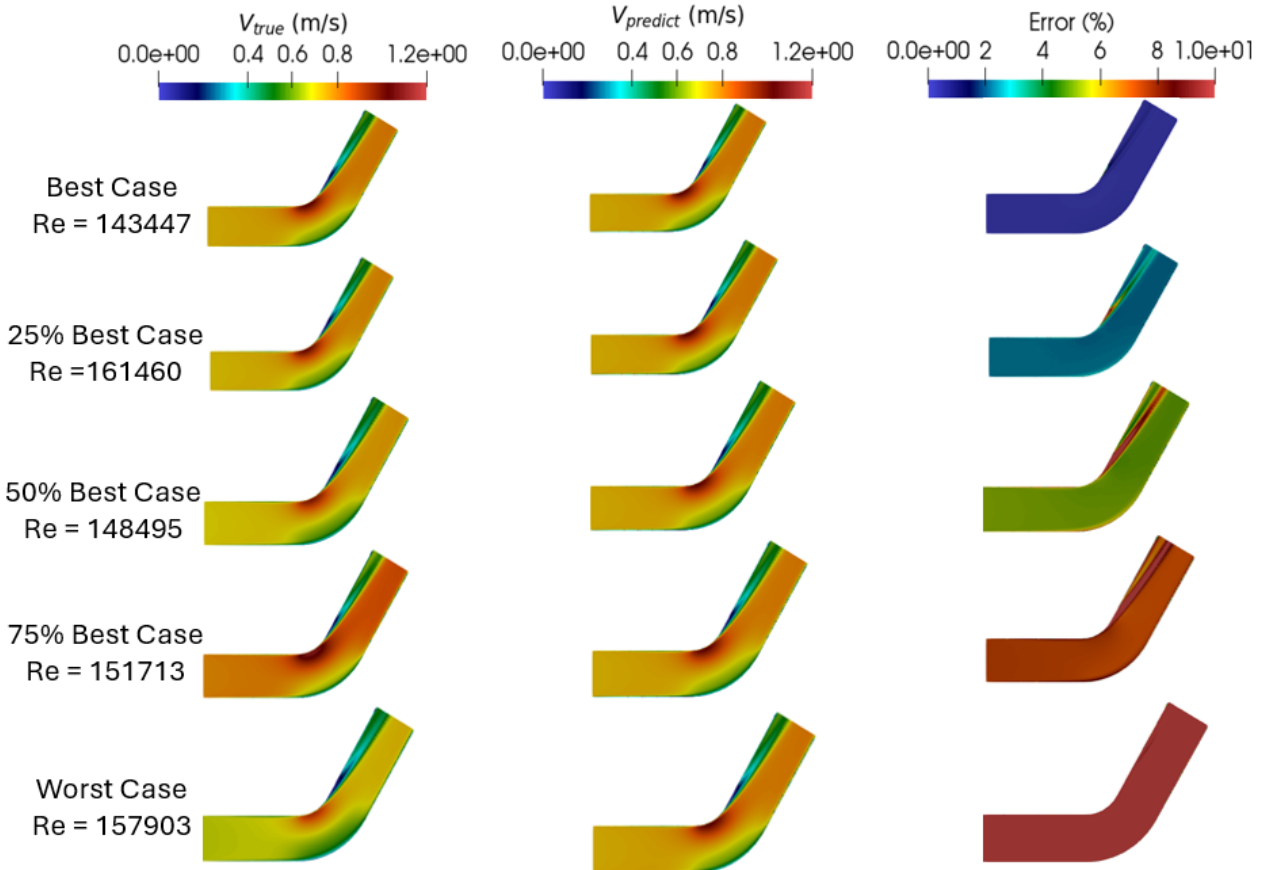


Figure 7: Visualization of true and predicted velocity at the focused plane.

Figure 9 represents the comparison of pressure between the CFD simulation and DeepONet. In the 120° elbow bend, centrifugal force causes the fluid to bulge towards the convex wall, decreasing flow rate and creating a high-pressure region. Conversely, the concave wall experiences contraction effects and increased velocity, resulting in a low-pressure zone. This pressure difference between the convex and concave sides drives a secondary flow from the convex to the concave wall along the bend's circumference. The investigation into pressure field predictions echoes previous observations regarding DeepONet's performance in capturing velocity fields. While the model demonstrates general proficiency, it encounters challenges in regions characterized by abrupt pressure transitions, particularly near the elbow joint where steep gradients and discontinuities are prevalent. In these areas, the model exhibits elevated prediction errors compared to regions with smoother pressure distributions. This aligns with the inherent difficulty of capturing sharp gradients and discontinuities using a data-driven model like DeepONet. The pressure behavior in these zones is strongly influenced by complex flow physics, whereas DeepONet primarily learns patterns from training data.

In general, the DeepONet model demonstrated a strong ability to accurately capture local fluctuations and patterns within the hydrodynamic variables. However, a disparity in prediction accuracy was observed across the different variables. Specifically, the highest errors were encountered in the turbulence kinetic energy predictions, followed by the pressure fields, with the velocity fields exhibiting the lowest errors. This suggests that the model's capacity to learn and generalize from the training data may be influenced by the inherent complexity and variability of the different flow variables. While DeepONet effectively captures the more readily observable velocity patterns, it struggles to achieve the same level of precision for the more nuanced and less directly measurable quantities such as turbulence kinetic energy and pressure. This could be attributed to the intricate physical relationships and nonlinear interactions governing these variables, which may not be fully captured by the current model architecture or training dataset.

Further research and model refinement, potentially incorporating additional physical constraints or specialized loss functions, may improve the accuracy of predictions for these more challenging flow variables.

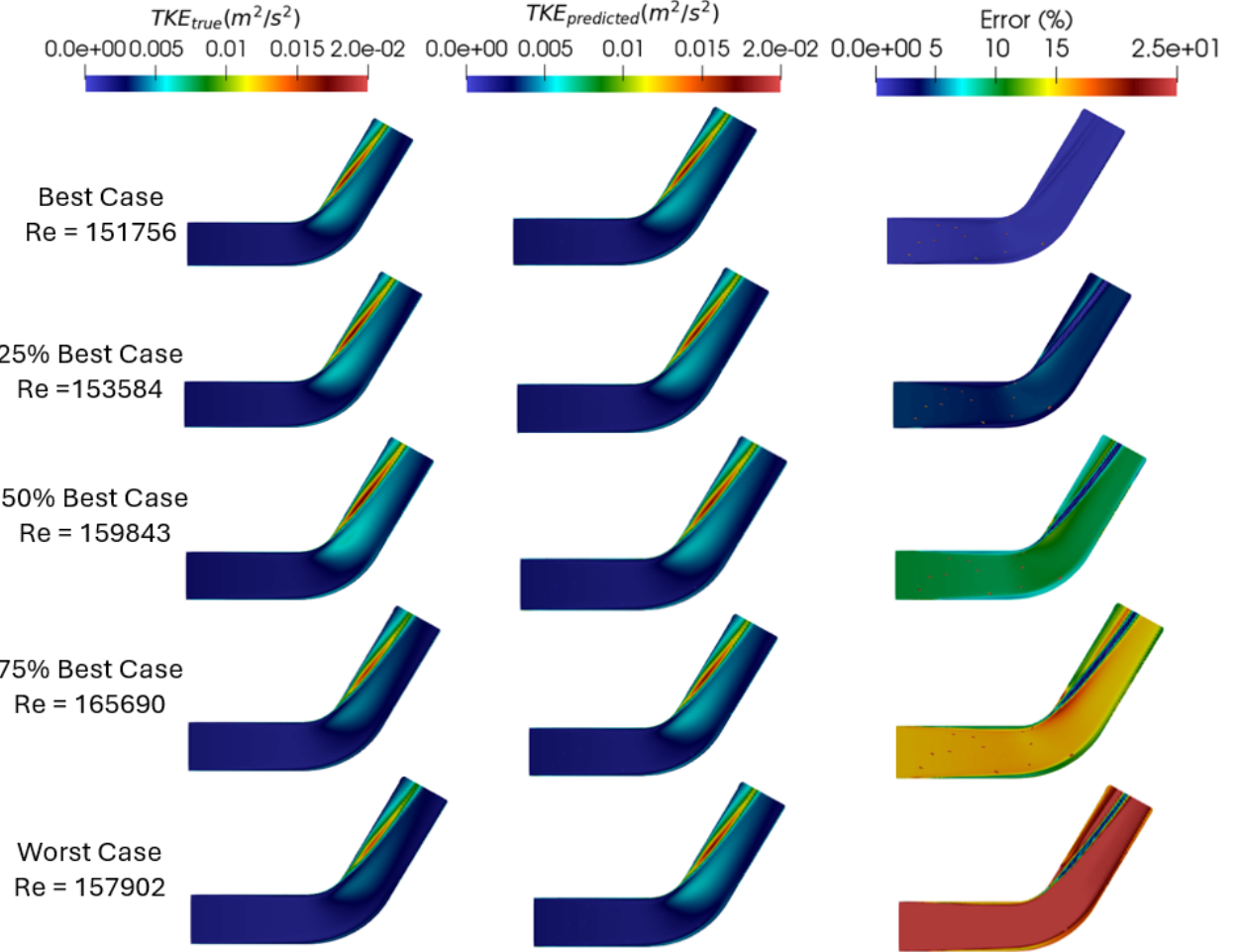


Figure 8: Visualization of true and predicted TKE at the focused plane.

4 Conclusion

In this study, we explored the application of DeepONet as a virtual sensing framework in the context of the prediction component of a digital twin for real-time degradation monitoring of thermal-hydraulic parameters within the primary coolant loop of an AP-1000 nuclear reactor. The results demonstrate that DeepONet, especially when enhanced with additional linear layers, provides highly reliable predictions for degradation-inducing parameters (pressure, velocity, and turbulence kinetic energy) across various operating conditions. Our study also revealed that DeepONet maintains consistent performance for real-time degradation monitoring across varying percentages of training data and different numbers of data points used for training. This robustness underscores the model's potential for deployment in scenarios with limited data or computational resources. Notably, DeepONet can make predictions 160,000 times faster than traditional finite element (FE) simulations, making it highly suited for real-time monitoring applications. However, the model faces challenges, particularly in accurately predicting turbulence kinetic energy, where it exhibited higher relative errors. This suggests that while DeepONet is a powerful tool, further refinement—possibly incorporating additional physical constraints or more sophisticated loss functions—could enhance its accuracy for more complex flow variables. Overall, this study demonstrates the feasibility and advantages of using DeepONet as a virtual sensor for monitoring coolant flow in nuclear reactors. By providing a scalable and cost-effective complement to physical sensors, DeepONet enhances the safety, reliability, and efficiency of nuclear reactors, paving the way for more advanced digital twin technologies in the nuclear industry. In future work, we will focus on improving the model's accuracy in predicting complex flow behaviors and exploring its applicability to other critical components of nuclear reactors.

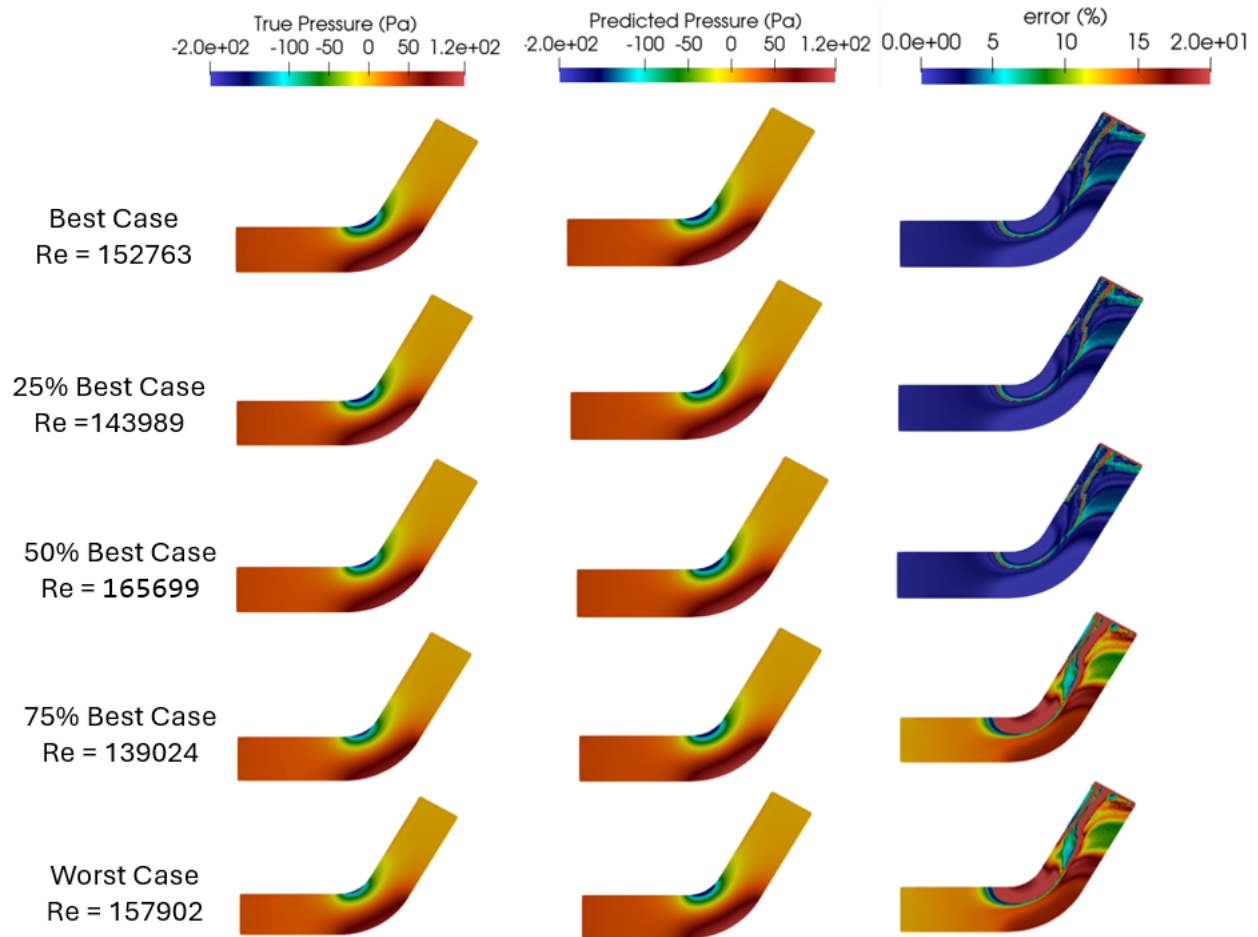


Figure 9: Visualization of true value and predicted Pressure in the focused plane.

Data and code availability

The data and code used and/or analysed during this study are available from the corresponding author on reasonable request.

Competing Interests

The authors declare no conflict of interest.

Author Contributions

Conceptualization: S.A., R.H. and K.K.; methodology: R.H.; Writing - original draft: R.H.; Review & Editing: All authors; Formal analysis: R.H.; Visualization: R.H. and K.K.; Data curation: R.H.; Supervision: S.A.; Project administration: S.A. and D.A.; All authors have read and agreed to the published version of the manuscript.

Declaration of Generative AI and AI-assisted Technologies in the Writing Process

During the preparation of this work, the author(s) used a Large Language Model (ChatGPT) for language editing and refinement. The AI was employed solely for improving the clarity and readability of the manuscript, and no content was generated or altered by the AI.

References

Yue Zou and Brian Derreberry. Thermal fatigue of pressurized water reactor coolant system loop drain line down horizontal elbow. *Volume 2: Nuclear Policy; Nuclear Safety, Security, and Cyber Security; Operating Plant Experience; Probabilistic Risk Assessments; SMR and Advanced Reactors*, 2020.

Jeffrey D. Keller and Alan J. Bilanin. Interim report on thermal cycling model development for representative unisolable piping configurations (mrp-81). 2002.

Michael Tunstall and John K. Harvey. On the effect of a sharp bend in a fully developed turbulent pipe-flow. *Journal of Fluid Mechanics*, 34:595 – 608, 1968.

Prasun Dutta, Sumit Kumar Saha, Nityananda Nandi, and Nairit Pal. Numerical study on flow separation in 90° pipe bend under high reynolds number by $k - \varepsilon$ modelling. *Engineering Science and Technology, an International Journal*, 19(2):904–910, 2016. ISSN 2215-0986.

Yukimaru Shimizu, Yoshiaki Futaki, and C. Samuel Martin. Secondary flow and hydraulic losses within sinuous conduits of rectangular cross section. *Journal of Fluids Engineering*, 114(4):593–600, 12 1992. ISSN 0098-2202.

Mahmood Khan, Muhammad Umer Farooq Awan, Khurram Lal, Muhammad Gulab, Shabbir Ahmed, and Zaheer Ahmed. Role of in-service inspections in nuclear power plants (npps). *The Nucleus*, 60(1):86–97, 2023.

Harleen Kaur Sandhu, Saran Srikanth Bodda, Erin Yan, Piyush Sabharwall, and Abhinav Gupta. A comparative study on deep learning models for condition monitoring of advanced reactor piping systems. *Mechanical Systems and Signal Processing*, 209:111091, 2024. ISSN 0888-3270.

Rui Han, Ping Li, and Ziyu Shi. Implementation strategy of predictive maintenance in nuclear power plant. In *2022 Prognostics and Health Management Conference (PHM-2022 London)*, pages 143–146, 2022.

Roman Davydov, Valentin Dudkin, Semen Logunov, and Alexander Bobyl. Optical method for controlling the flow rate of the coolant in nuclear reactors. In *2021 International Conference on Electrical Engineering and Photonics (EExPolytech)*, pages 179–183, 2021.

R. D. Tokarz. Coolant monitoring apparatus for nuclear reactors, 1983.

Yasuo Kuroze, M. Yamada, Hideo Shintani, A. Nunoko, and R. Murakami. Continuous measurement of iodine concentration in the primary coolant of a nuclear power plant. *1996 IEEE Nuclear Science Symposium. Conference Record*, 1:135–138 vol.1, 1996.

Derek Lister and Shunsuke Uchida. Determining water chemistry conditions in nuclear reactor coolants. *Journal of Nuclear Science and Technology*, 52, 04 2015.

Fredrik Jensen, Eiji Takada, Masaharu Nakazawa, Hiroyuki Takahashi, T. Iguchi, Tsunemi Kakuta, and Satoshi Yamamoto. Development of a distributed monitoring system for temperature and coolant leakage. 01 1996.

U.S. Nuclear Regulatory Commission. Ce technology cross training r325c.- chapter 02.1 - reactor coolant system piping. Technical Report ML11251A014, U.S. Nuclear Regulatory Commission, 2011.

Raisa Bentay Hossain, Kazuma Kobayashi, and Syed Bahauddin Alam. Sensor degradation in nuclear reactor pressure vessels: the overlooked factor in remaining useful life prediction. *npj Materials Degradation*, 8(1):71, 2024.

Niharika Karnik, Congjian Wang, Palash K. Bhowmik, Joshua J. Cogliati, Silvino A. Balderrama Prieto, Changhu Xing, Andrei A. Klishin, Richard Skifton, Musa Moussaoui, Charles P. Folsom, Joe J. Palmer, Piyush Sabharwall, Krithika Manohar, and Mohammad G. Abdo. Leveraging optimal sparse sensor placement to aggregate a network of digital twins for nuclear subsystems. *Energies*, 17(13), 2024.

Jingyu Wu, Mohan Wang, Kehao Zhao, Sheng Huang, Mohamed A. S. Zaghloul, Rongtao Cao, David Carpenter, Guiqiu Zheng, Steven Derek Rountree, and Kevin P. Chen. Distributed fiber sensors with high spatial resolution in extreme radiation environments in nuclear reactor cores. *Journal of Lightwave Technology*, 39(14):4873–4883, 2021.

P. Ferdinand, S. Magne, O. Roy, V. Dewynter Marty, S. Rougeault, and M. Bugaud. *Optical Fiber Sensors for the Nuclear Environment*, pages 205–226. Springer US, Boston, MA, 2000. ISBN 978-0-306-47099-8.

Mengjie Zhao, Cees Taal, Stephan Baggerohr, and Olga Fink. Virtual sensor for real-time bearing load prediction using heterogeneous temporal graph neural networks. *arXiv preprint arXiv:2404.02304*, 2024a.

Mengjie Zhao, Cees Taal, Stephan Baggerohr, and Olga Fink. Graph neural networks for virtual sensing in complex systems: Addressing heterogeneous temporal dynamics. *arXiv preprint arXiv:2407.18691*, 2024b.

Keivan Faghah Niresi, Hugo Bissig, Henri Baumann, and Olga Fink. Physics-enhanced graph neural networks for soft sensing in industrial internet of things. *arXiv preprint arXiv:2404.08061*, 2024.

Shan-Bin Sun, Yuan-Yuan He, Si-Da Zhou, and Zhen-Jiang Yue. A data-driven response virtual sensor technique with partial vibration measurements using convolutional neural network. *Sensors*, 17(12):2888, 2017.

Daniele Masti, Daniele Bernardini, and Alberto Bemporad. A machine-learning approach to synthesize virtual sensors for parameter-varying systems. *Eur. J. Control*, 61:40–49, 2021.

Andreas B. Ofner, Jonas Sjöblom, Stefan Posch, Markus Neumayer, Bernhard C. Geiger, and Stephan Schmidt. Virtual sensors in small engines – previous successes and promising future use cases. *SAE Technical Paper Series*, 2023.

Rizwan Ahmed, Pak Sukyoung, Gyungyoung Heo, Jung-Taek Kim, Seop Hur, Soo Yong Park, and Kwang-II Ahn. Development of virtual sensor networks to support accident monitoring systems. *Annual Conference of the PHM Society*, 5(1), October 2013. ISSN 2325-0178.

Lichuan Liu, Sen M. Kuo, and Meng Chu Zhou. Virtual sensing techniques and their applications. In *Proceedings of the 2009 IEEE International Conference on Networking, Sensing and Control, ICNSC 2009*, pages 31–36.

Yusra Barmaz. The rise of virtual sensors, 2023. URL <https://etech.iec.ch/issue/2023-01/the-rise-of-virtual-sensors>.

J. Sevilla and C. Pulido. Virtual industrial sensors through neural networks. demonstration examples in nuclear power plants. In *IMTC/98 Conference Proceedings. IEEE Instrumentation and Measurement Technology Conference. Where Instrumentation is Going (Cat. No.98CH36222)*, volume 1, pages 293–297, 1998.

Ramakrishna Tipireddy, Megan E. Lerchen, and Pradeep Ramuhalli. Virtual sensors for robust on-line monitoring (olm) and diagnostics. In *Proceedings of the 10th International Topical Meeting on Nuclear Plant Instrumentation, Control and Human Machine Interface Technologies (NPIC & HMIT 2017)*, pages 719–728, 2017.

Kazuma Kobayashi and Syed Bahauddin Alam. Explainable, interpretable, and trustworthy AI for an intelligent digital twin: A case study on remaining useful life. *Engineering Applications of Artificial Intelligence*, 129:107620, 2024a.

Kazuma Kobayashi and Syed Bahauddin Alam. Deep neural operator-driven real-time inference to enable digital twin solutions for nuclear energy systems. *Nature Scientific reports*, 14(1):2101, 2024b.

Kazuma Kobayashi, James Daniell, and Syed Bahauddin Alam. Improved generalization with deep neural operators for engineering systems: Path towards digital twin. *Engineering Applications of Artificial Intelligence*, 131:107844, 2024a.

Hussain Mohammed Dipu Kabir and Syed Bahauddin Alam. Hardware based realtime, fast and highly secured communication using FPGA. In *2010 IEEE International Conference on Information Theory and Information Security*, pages 452–457. IEEE, 2010.

Kazuma Kobayashi, Dinesh Kumar, and Syed Bahauddin Alam. AI-driven non-intrusive uncertainty quantification of advanced nuclear fuels for digital twin-enabling technology. *Progress in Nuclear Energy*, 172:105177, 2024b.

Dominik Martin, Niklas Kühl, and Gerhard Satzger. Virtual sensors. *Bus Inf Syst Eng*, 63(3):315–323, March 2021. ISSN 1867-0202.

Dinesh Kumar, Mariapia Marchi, Syed Bahauddin Alam, Carlos Kavka, Yao Koutsawa, Gaston Rauchs, and Salim Belouettar. Multi-criteria decision making under uncertainties in composite materials selection and design. *Composite Structures*, 279:114680, 2022.

Lu Lu, Pengzhan Jin, Guofei Pang, Zhongqiang Zhang, and George Em Karniadakis. Learning nonlinear operators via deepenet based on the universal approximation theorem of operators. *Nature machine intelligence*, 3(3):218–229, 2021.

Zongyi Li, Nikola Kovachki, Kamyar Azizzadenesheli, Burigede Liu, Kaushik Bhattacharya, Andrew Stuart, and Anima Anandkumar. Fourier neural operator for parametric partial differential equations, 2020.

M. Raissi, P. Perdikaris, and G.E. Karniadakis. Physics-informed neural networks: A deep learning framework for solving forward and inverse problems involving nonlinear partial differential equations. *Journal of Computational Physics*, 378:686–707, 2019. ISSN 0021-9991.

Lu Lu, Xuhui Meng, Shengze Cai, Zhiping Mao, Somdatta Goswami, Zhongqiang Zhang, and George Em Karniadakis. A comprehensive and fair comparison of two neural operators (with practical extensions) based on fair data. *Computer Methods in Applied Mechanics and Engineering*, 393:114778, 2022. ISSN 0045-7825.

Seid Koric and Diab W. Abueidda. Data-driven and physics-informed deep learning operators for solution of heat conduction equation with parametric heat source. *International Journal of Heat and Mass Transfer*, 203:123809, 2023. ISSN 0017-9310.

Junyan He, Shashank Kushwaha, Jaewan Park, Seid Koric, Diab Abueidda, and Iwona Jasiuk. Sequential deep operator networks (s-deepenet) for predicting full-field solutions under time-dependent loads. *Engineering Applications of Artificial Intelligence*, 127, January 2024. ISSN 0952-1976.

Ihn Namgung and Nguyen Hoang Giang. Investigation of burst pressures in pwr primary pressure boundary components. *Nuclear Engineering and Technology*, 48(1):236–245, 2016a. ISSN 1738-5733.

Ihn Namgung and Nguyen Hoang Giang. Investigation of burst pressures in pwr primary pressure boundary components. *Nuclear Engineering and Technology*, 48(1):236–245, 2016b.

Farid Ahmed, Md Hasan Nasrullah, Istiak Ahmad, Kazuma Kobayashi, and Syed Bahauddin Alam. Enhancing thermo-hydraulic performance in dimpled channels with wavy tape inserts for heat pipe & heat exchanger design with complex energy systems. *Case Studies in Thermal Engineering*, page 104583, 2024.

F Ahmed, Achiya Khanam, L Samylingam, Navid Aslfattahi, and R Saidur. Assessment of thermo-hydraulic performance of mxene-based nanofluid as coolant in a dimpled channel: a numerical approach. *Journal of Thermal Analysis and Calorimetry*, 147(22):12669–12692, 2022.

F Ahmed, Md Atrehar Abir, PK Bhowmik, V Deshpande, and AS Mollah. Thermohydraulic performance of water mixed al₂o₃, tio₂ and graphene-oxide nanoparticles for nuclear fuel triangular subchannel. *Thermal Science and Engineering Progress*, 24:100929, 2021.

Gregory Francis Homicz. Computational fluid dynamic simulations of pipe elbow flow. Technical report, Sandia National Laboratories (SNL), Albuquerque, NM, and Livermore, CA . . ., 2004.

Pengzhan Jin, Shuai Meng, and Lu Lu. Mionet: Learning multiple-input operators via tensor product. *SIAM Journal on Scientific Computing*, 44(6):A3490–A3514, 2022.

Junyan He, Seid Koric, Shashank Kushwaha, Jaewan Park, Diab Abueidda, and Iwona Jasiuk. Novel deeponet architecture to predict stresses in elastoplastic structures with variable complex geometries and loads. *Computer Methods in Applied Mechanics and Engineering*, 415:116277, 2023. ISSN 0045-7825.